Quasicrystalline second-order topological semimetals

Rui Chen,[1] Bin Zhou,[1] and Dong-Hui Xu[2,3,*]
[1]*Department of Physics, Hubei University, Wuhan 430062, China*
[2]*Department of Physics, Chongqing University, Chongqing 400044, China*
[3]*Chongqing Key Laboratory for Strongly Coupled Physics, Chongqing University, Chongqing 400044, China*

(Received 9 July 2023; accepted 1 November 2023; published 14 November 2023)

Three-dimensional higher-order topological semimetals in crystalline systems exhibit higher-order Fermi arcs on one-dimensional hinges, challenging the conventional bulk-boundary correspondence. However, the existence of higher-order Fermi arc states in aperiodic quasicrystalline systems remains uncertain. In this paper, we present the emergence of three-dimensional quasicrystalline second-order topological semimetal phases by vertically stacking two-dimensional quasicrystalline second-order topological insulators. These quasicrystalline topological semimetal phases are protected by rotational symmetries forbidden in crystals, and are characterized by topological hinge Fermi arcs connecting fourfold degenerate Dirac-like points in the spectrum. Our findings reveal an intriguing class of higher-order topological phases in quasicrystalline systems, shedding light on their unique properties.

DOI: 10.1103/PhysRevB.108.195306

I. INTRODUCTION

Symmetry-protected topological phases of matter have emerged as a major new theme in modern condensed-matter physics in the past nearly two decades. While the discovery of topological insulators initially sparked interest in this field, recent focus has shifted towards exploring higher-order topological insulators [1–5]. Unlike traditional topological insulators, higher-order topological insulators exhibit unconventional bulk-boundary correspondence, allowing for the existence of gapless boundary excitations of higher codimensions. For example, a second-order topological insulator (SOTI) in two dimensions hosts robust gapless boundary modes localized at its zero-dimensional corners, dubbed corner modes [1], while three-dimensional (3D) SOTIs support gapless boundary modes confined to their one-dimensional hinges [2]. In addition to higher-order topological insulators, higher-order topological semimetals have also been identified. These semimetals, including higher-order Dirac semimetals and higher-order Weyl semimetals, exhibit exotic hinge Fermi arcs that connect the projected nodes on the hinges, distinguishing them from conventional Dirac and Weyl semimetals [6–18].

Initially, topological phases were observed in crystalline materials. However, more recently, researchers have extended these phases to aperiodic quasicrystalline systems, which lack discrete translational symmetry [19–54]. The absence of translational symmetry allows for the presence of rotational symmetries that are prohibited in crystals. This property enables the existence of new topological phases without crystalline counterparts, such as two-dimensional (2D) SOTIs protected by eightfold [33,34] and twelvefold [26,35] rotational symmetries. Moreover, a 3D time-reversal symmetry (TRS) breaking gapless topological phase hosting Weyl-like points has been proposed in a quasicrystal stack of Chern insulators [55]. However, gapless phases with higher-order topology in quasicrystalline systems have yet to be discovered. This knowledge gap motivates us to explore the possibility of gapless quasicrystalline higher-order topological phases using a stacking approach with 2D quasicrystalline SOTIs. It has been demonstrated that stacking 2D topological materials provides a natural way of realizing 3D topological phases. This approach has been successful in achieving various topological phases, including Weyl semimetals [56], axion insulators [57–61], hinged quantum spin Hall insulators [62,63], and high-Chern number quantum anomalous Hall insulators [64].

In this paper, we present the discovery of a quasicrystalline second-order topological semimetal (SOTSM) phase obtained by stacking 2D quasicrystalline SOTIs along the vertical direction (Fig. 1). The distinctive feature of the quasicrystalline SOTSM is the presence of rotation-symmetry-protected topological hinge Fermi arcs that terminate at fourfold degenerate Dirac-like points in the spectrum. The C_n^z-symmetric quasicrystalline SOTSM can support n topological hinge Fermi arcs (see the second column in Fig. 1), inheriting their topological nature from C_n^z-symmetric quasicrystalline SOTI hosting n corner modes (see the first column in Fig. 1). The number n can be four [Figs. 1(a) and 1(b)], as allowed in crystalline systems [9–13,16], but it can also be eight [Figs. 1(c) and 1(d)] and twelve [Figs. 1(e) and 1(f)], which are typically forbidden in crystalline systems. The hinge Fermi arcs associated with eightfold and twelvefold rotational symmetries make SOTSMs distinct from crystalline higher-order Dirac [10,13] and Weyl semimetals [17,18]. Furthermore, we present the phase diagram of the stacked systems and identify a 3D quasicrystalline SOTI phase in addition to the

*donghuixu@cqu.edu.cn

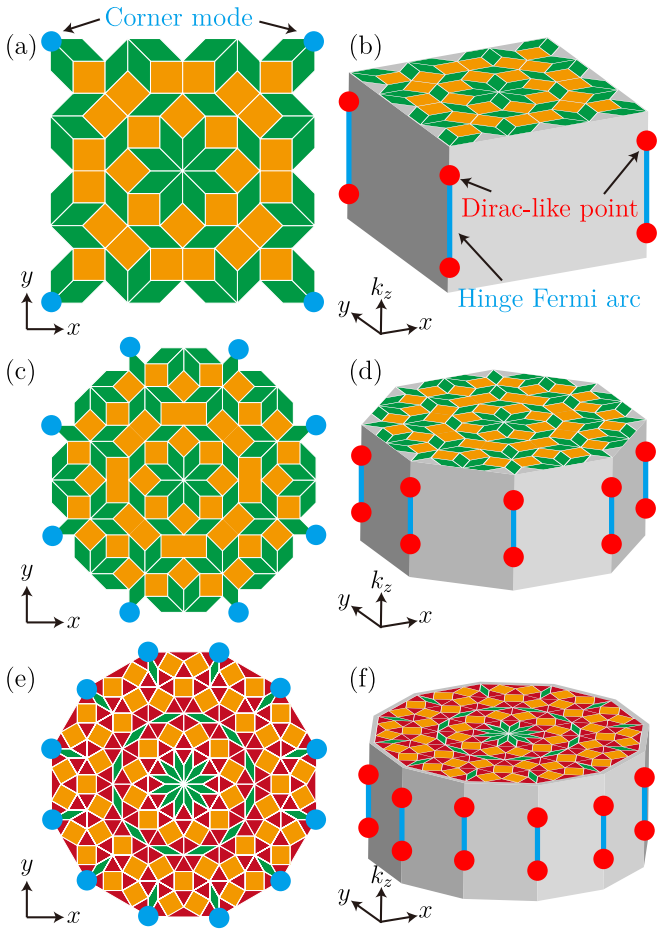

FIG. 1. Schematic illustrations of (a) AB-tiling square, (c) AB-tiling octagonal, and (e) Stampfli-tiling dodecagonal quasicrystals. AB-tiling quasicrystal consists of two types of primitive tiles: square tiles (yellow) and rhombus tiles (green) with a small angle 45°. Stampfli-tiling quasicrystal consists of three types of primitive tiles: square tiles (yellow), regular triangle tiles (red), and rhombus tiles (green) with a small angle 30°. In (a), (c), and (e), the side lengths (the white lines) of the polygons are taken as the length unit with $a = 1$. 2D quasicrystalline SOTIs support (a) four, (c) eight, and (e) twelve rotation-symmetry-protected zero-energy corner modes (the cyan points). A simple stack of the 2D quasicrystalline SOTIs gives rise to 3D quasicrystalline SOTSMs with (b) four, (d) eight, and (f) twelve rotation-symmetry-protected hinge Fermi arc states (the cyan lines) connecting the Dirac-like points (the red points) in the spectrum.

quasicrystalline SOTSM phase. Finally, we show that the disclination-induced bound states can further reveal the topological nature of the quasicrystalline SOTSM phase.

This paper is organized as follows. We first give a simple review of 2D quasicrystalline SOTI in Sec. II and show a stack of it gives rise to the 3D quasicrystalline SOTSM phase with Dirac-like points in the spectrum in Sec. III. A detailed discussion on Dirac-like points is presented in Sec. IV. Subsequently, we illustrate the phase diagram of the stacked quasicrystalline system in Sec. V and investigate the disclination-induced bound state in Sec. VI. We summarize our conclusions and discuss possible experimental schemes for the quasicrystalline SOTSM phase in Sec. VII.

II. REVIEW OF 2D QUASICRYSTALLINE SOTIS

2D quasicrystalline SOTIs had been proposed in eightfold symmetric Ammann-Beenker-tiling (AB-tiling) quasicrystal [33,34] [Figs. 1(a) and 1(c)] and twelvefold symmetric Stampfli-tiling quasicrystal [35] [Fig. 1(e)]. The AB-tiling quasicrystal consists of two types of primitive tiles: square tiles (yellow) and rhombus tiles (green) with a small angle 45°. The Stampfli-tiling quasicrystal consists of three types of primitive tiles: square tiles (yellow), regular triangle tiles (red), and rhombus tiles (green) with a small angle 30°.

In the tight-binding model, the lattice sites are placed on the vertices of each tile. The Hamiltonian of the 2D quasicrystalline SOTI contains two parts, $H(M) = H_{1st}(M) + H_m$ [33]. The first part denotes a 2D first-order topological insulator protected by TRS

$$H_{1st}(M) = -\sum_{j\neq k} \frac{Z(r_{jk})}{2} [it_1(s_3\tau_1 \cos\phi_{jk} + s_0\tau_2 \sin\phi_{jk}) + t_2 s_0\tau_3]c_j^\dagger c_k + \sum_j (M + 2t_2) s_0\tau_3 c_j^\dagger c_j, \quad (1)$$

where $c_{j\alpha}^\dagger = (c_{j\alpha\uparrow}^\dagger, c_{j\alpha\downarrow}^\dagger)$ are electron creation operators at site j with the orbital α. t_1 and t_2 are hopping amplitudes, and M denotes the Dirac mass, together with t_2, determining the first-order topology. $s_{1,2,3}$ and $\tau_{1,2,3}$ are the Pauli matrices acting on the spin and orbital spaces, respectively. s_0 is the 2×2 identity matrix. ϕ_{jk} is the azimuthal angle of the bond between site j and k with respect to the horizontal direction. $Z(r_{jk}) = e^{1-r_{jk}/\xi}$ is the spatial decay factor of hopping amplitudes with the decay length ξ. The second part is a TRS breaking Wilson mass term, which is

$$H_m(\eta) = g\sum_{j\neq k} \frac{Z(r_{jk})}{2} \cos(\eta\phi_{jk}) s_1\tau_1 c_j^\dagger c_k, \quad (2)$$

where g and η describe the magnitude and varying period of the Wilson mass, respectively. $H_m(\eta)$ are responsible for higher-order topology [33,65]. In the subsequent calculations, we fix the side length of the tiles as $a = 1$ (white lines connecting the vertices in Fig. 1) and $\xi = t_1 = 1$.

For $\eta = 2, 4, 6$, the Wilson mass gives rise to the SOTI phases in quasicrystals hosting four, eight, and twelve corner modes protected by the combined symmetry $C_4^z U$ [33,65], $C_8^z U$ [33], and $C_{12}^z U$ [35], respectively, where C_n^z is the n-fold rotational operation, and U could be the TRS operation $T = is_2\tau_0 K$ or the mirror symmetry operation $m_z = s_3\tau_0$. K is the complex conjugation operator. Additionally, these corner modes are pinned to zero energy due to the existence of particle-hole symmetry.

To demonstrate the higher-order topological boundary states, we choose symmetry-compatible edges in our calculations. The emergence of the zero-energy corner modes can be simply understood as follows [33,37,66]: g opens a gap in the first-order topological edge states and then induces Wilson mass kinks near the boundary. The effective Wilson mass on the edge is determined by both the factor η and the edge orientation. A corner mode appears when the adjacent two edges host opposite Wilson masses. If one corner mode $|\psi_c\rangle$ appears at $\mathbf{r}_c$, where the Wilson mass flips the sign, then the

$C_n^z U$ symmetry ensures that the number of corner modes is n. This is because $C_n^z U|\psi_c\rangle$ is also the eigenstate of the system, which is localized at another corner by rotating $\mathbf{r}_c$ by an angle of $2\pi/n$.

III. 3D QUASICRYSTALLINE SOTSMs

3D crystalline SOTSMs have been constructed by stacking 2D crystalline SOTIs along the vertical direction [6–16]. 3D quasicrystalline SOTSM phases can be achieved in a similar manner, i.e., by periodically staking 2D quasicrystalline SOTIs with an orbital-dependent hopping $t_z s_0 \tau_3$ on each site [55]. After Fourier transformation applied to the vertical direction z, the 3D stacked Hamiltonian can be expressed as

$$H_{3D} = \sum_{k_z} H(M - 2t_z \cos k_z). \tag{3}$$

The conduction and valence bands of in this model have double degeneracy because of the presence of the combination of TRS and inversion symmetry PT [12,67], where $P = s_0\tau_3$ is the inversion-symmetry operator. It is necessary to point out that when $\eta = 2$, applying the stacked Hamiltonian to periodic cubic lattices will give birth to a 3D crystalline SOTSM [12,67] (see Appendix A) with four hinge Fermi arcs connecting the projection of fourfold degenerate Dirac points that are well defined in the momentum space. Next, we investigate the situation where the Hamiltonian is defined on a stack of 2D quasicrystals.

A. $\eta = 2$

We first consider a 3D quasicrystal [Fig. 1(b)] by stacking 2D AB-tiling quasicrystals with the square-shaped boundary [Fig. 1(a)] and set the varying period of Wilson mass $\eta = 2$. Figure 2(a) shows the spectral function $\mathcal{A}(E_F, k_z)$ of the 3D quasicrystalline system with open-boundary condition in the xy plane. We can see that the bulk conduction and valence bands touch at two discrete points $k_z = \pm k_z^1$ where the energy gap is closed, indicating a semimetal phase. Importantly, fourfold degenerate zero-energy flat band boundary states emerge in the region $|k_z| > k_z^1$, describing hinge Fermi arc states in this semimetal phase. Figure 2(c) displays the probability density distribution of the zero-energy states at $k_z = -2$ [marked by the green star in Fig. 2(a)].

Figure 2(b) illustrates the spectral function of the quasicrystalline system with periodic boundary conditions along all the directions. The periodic boundary condition in the xy plane is achieved by treating the system as a crystal with a supercell periodicity. Moreover, we observe no significant change in the results as the system size continues to grow. Therefore, we expect that the supercell approximation can capture the essential feature of the bulk states in the quasicrystalline system. Comparing to the spectral function under open boundary condition in Fig. 1(a), the zero-energy flat band boundary states disappear, further confirming that the zero-energy modes in between $\pm k_z^1$ are hinge Fermi arc states. Moreover, for crystalline topological Dirac semimetals with hinge Fermi arcs, there are already several studies showing that the bulk topology can be characterized by the Wilson loop [10] or filling anomaly based on symmetry indicators

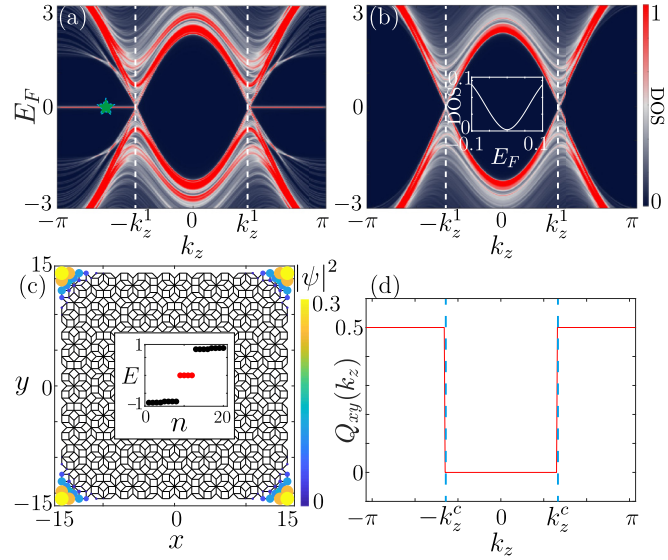

FIG. 2. Spectral function of the stacked AB-tiling quasicrystal with square-shaped disk [see Fig. 1(b)] as a function of k_z, under (a) open boundary condition in xy plane and periodic boundary condition along the z direction, and (b) periodic boundary conditions along all the three directions. (c) The probability distribution of the zero-energy modes with $k_z = -2$ [marked by the green star in (a)]. (d) The quadrupole moment as a function of k_z, calculated under periodic boundary conditions along all the three directions. The parameters are taken as $M = -2$, $t_2 = 1$, $g = 1$, and $t_z = 1.5$. The lattice site number is 1257.

[9]. However, these indicators calculated in the momentum space are no longer applicable in quasicrystals due to the absence of the transitional symmetry. We find that the higher-order topology of the hinge Fermi arcs is revealed by the quantized quadrupole moment $Q_{xy} = 0.5$ for $|k_z| > k_z^1$ [Fig. 2(d)]. Therefore, the system is identified as a quasicrystalline SOTSM.

The bulk spectral function versus k_z exhibits a linear dispersion near the gap-closing points at $\pm k_z^1$ [Fig. 2(b)]. Meanwhile, the density of states around the gap-closing points is parabolic, as shown in the inset of Fig. 2(b), which identifies the well-known bulk signatures of Dirac points in crystalline systems [68,69]. These features suggest that the gapless points in the present system are Dirac points in quasicrystals. However, as discussed in Sec. IV, a more detailed analysis reveals that the situation is complex.

B. $\eta = 4$ and $\eta = 6$

Now, we come to the case of $\eta = 4$ and $\eta = 6$, which can give rise to 2D quasicrystalline SOTIs without crystalline counterpart [33,35]. Here, the 3D quasicrystalline systems are stacked by the AB-tiling octagonal quasicrystal [Figs. 1(c) and 1(d)] and the Stampfli-tiling dodecagonal quasicrystal [Figs. 1(e) and 1(f)], respectively. Figures 3(a) and 3(b) show the spectral function $\mathcal{A}(E_F, k_z)$ of the two 3D quasicrystalline systems with open boundary condition in the xy plane and periodic boundary condition along the vertical direction. The spectral functions look similar to that shown in Fig. 2(a); however, the degeneracy of zero-energy modes is different.

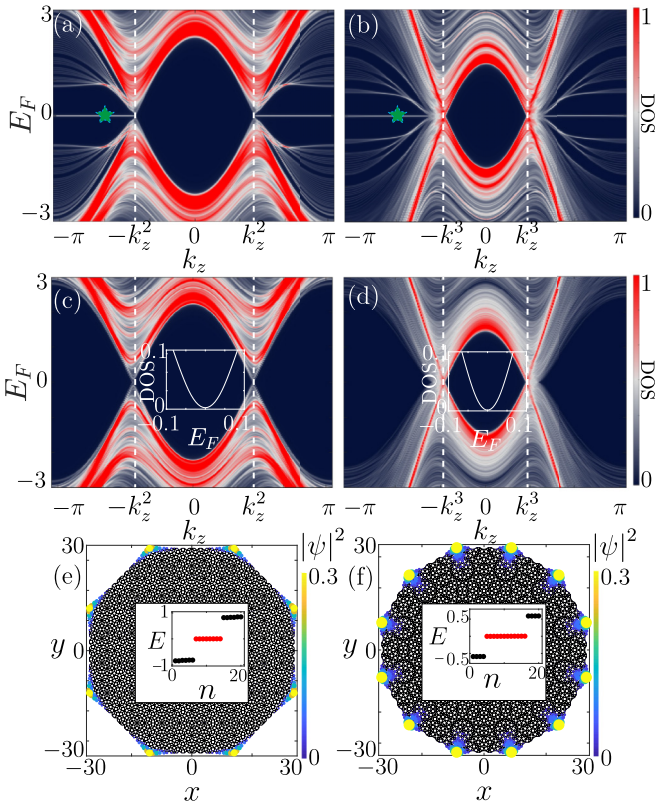

FIG. 3. Spectral function of the quasicrystalline octagonal system [see Fig. 1(d)] as a function of k_z with (a) open boundary conditions along the in-plane x and y directions and periodic boundary condition along the z direction, and (c) periodic boundary conditions along all the three directions. The lattice site number is 4713. (e) The probability distribution of the zero-energy modes in the quasicrystalline octagonal system with $k_z = -2$ [marked by the green star in (a)]. (b), (d), and (f) are the same as (a), (c), and (e), except that they describe the quasicrystalline dodecagonal system [see Fig. 1(f)] with the lattice site number is 4105. The parameters are $M = -2, t_2 = 1, g = 1, t_z = 1.5$ in (a), (c), and (e), and $M = -3$, $t_2 = 2, g = 2, t_z = 2$ in (b), (d), and (f).

These zero-energy flat-band boundary modes in the region $|k_z| > k_z^1$ are hinge Fermi arc states traveling on the hinges of 3D octagonal/dodecagonal quasicrystals. This can be observed more clearly in Figs. 3(e) and 3(f), which show the energy spectra and the probability distributions of the zero-energy modes for fixed k_z marked by the green stars shown in Figs. 3(a) and 3(a), respectively. Apparently, the hinge Fermi arc states are inherited from the C_n^z-symmetric corner modes in quasicrystalline SOTIs, where $n = 8$ in the AB-tiling octagonal quasicrystal and $n = 12$ in the Stampfli-tiling dodecagonal quasicrystal.

To diagonalize the electronic structure of bulk state, we plot the spectral function under periodic boundary conditions along all the three directions in Figs. 3(c) and 3(d). As seen in the case with $\eta = 2$, similar phenomena are observed, such as the disappearance of zero-energy hinge arcs, a linear dispersion along k_z, and the quadratic density of states around the gap-closing points.

Therefore, our study demonstrates that stacking 2D quasicrystals can result in the emergence of an exotic topological phase of matter, i.e., the quasicrystalline SOTSMs, which possesses eight and twelve hinge Fermi arcs protected by forbidden rotation symmetries in crystalline systems. Our findings highlight the potential for stacking 2D quasicrystals and expand our understanding of condensed-matter physics.

IV. DIRAC-LIKE POINTS

Upon initial inspection, the gap-closing points near $k_z = \pm k_z^{1,2,3}$ shown in Figs. 2(b), 3(c), and 3(d) are reminiscent of the Dirac point characterized by the massless Dirac equation. They both exhibit a linear dispersion along k_z and a unique quadratic density of state near the gap-closing points. However, a closer inspection of the spectrum reveals that the gap-closing points in quasicrystalline SOTSMs are distinct from those in crystalline second-order topological Dirac semimetals (SODSMs).

Figure 4(a) shows the spectrum near the gap-closing point k_z^1 in the SOTSM of $\eta = 2$ under periodic boundary conditions along all the directions [see Fig. 2(b)]. There appear three band-crossing points, which is quite different from the crystalline SODSM phase that hosts only one band-crossing point [Fig. 7(e)]. Figures 4(b) and 4(e) show the wave function of the states marked by the red and green stars in Fig. 4(a), respectively. One of the band crossing is dominated by the local patch containing three square tiles and two rhombus tiles [Figs. 4(b) and 4(c)], and the other band crossing is dominated by the local patch containing six rhombus tiles [Figs. 4(d) and 4(e)]. The appearance of multiple band-crossing points is because gap closes at different k_z for distinct kinds of local patches. This phenomenon is attributed to the absence of discrete translational symmetry in quasicrystalline systems.

For the AB-tiling octagonal quasicrystal with $\eta = 4$, the spectrum lacks multiple band-crossing points, but exhibits a tiny energy gap [Fig. 4(f)]. The tiny energy gap persists even with larger system sizes [Fig. 4(g)]. The tiny energy gap remains persistent and does not diminish even with further increases in size. The reason for this energy gap remains elusive and warrants additional investigation. For the Stampfli-tiling quasicrystal with $\eta = 6$, the spectrum is similar to the case with $\eta = 2$, except that there appear more band crossings. This is because there are more different patterns of local patches in Stampfli-tiling quasicrystal.

Although the gap-closing points in quasicrystalline SOTSMs manifest several similarities compared to the Dirac points in crystalline SODSMs. However, we found the fine structure of the gap-closing points due to the absence of translational symmetry by further checking the spectrum. Therefore, we dub these gap-closing points in the quasicrystalline SOTSM phase as Dirac-like points.

V. PHASE DIAGRAM

We present the topological phase diagram of the stacked quasicrystal system in this section. Figures 5(a) and 5(b) show $\ln E_g$ and Q_{xy} as functions of the momentum k_z and the parameter M for the AB-tiling quasicrystalline square system with $\eta = 2$. E_g is the value of the energy gap obtained under periodic boundary conditions along all the three directions. Each point along the white line corresponds

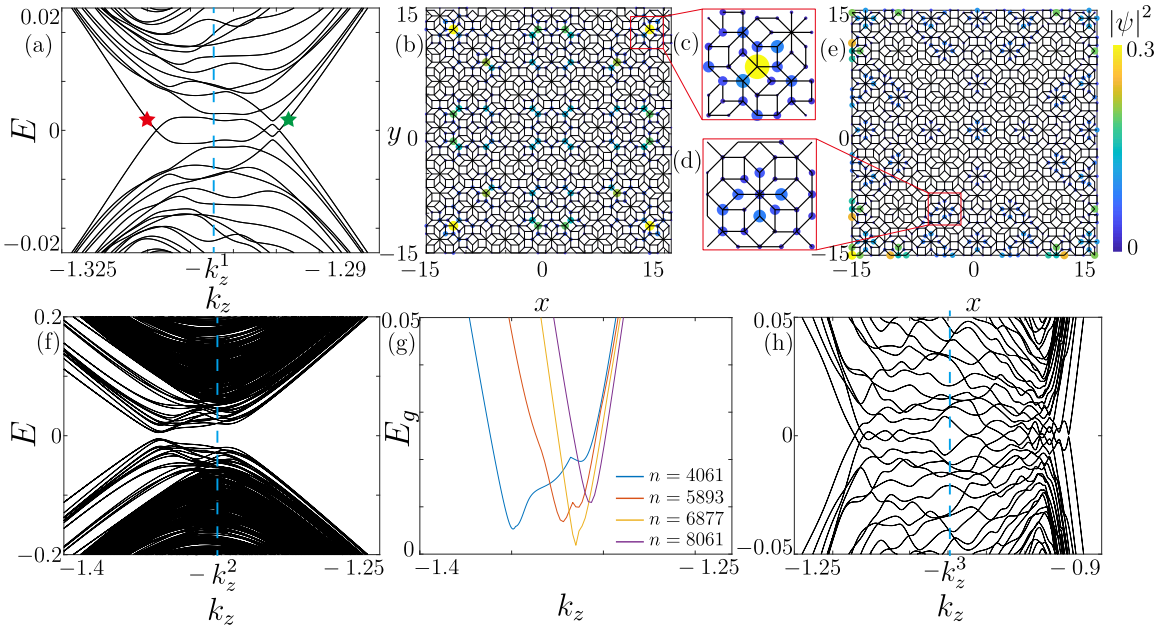

FIG. 4. (a) Energy spectrum vs k_z of the quasicrystalline system near $-k_z^1$ with $\eta = 2$ [see Fig. 2(b)]. The lattice number is 1257. (b) and (e) correspond to the probability distributions of the states marked by the red and green stars in (a), respectively. (c) and (d) show that the probability distributions in (b) and (e) are mainly distributed at two different kinds of local patches. (f) Spectrum of the quasicrystalline system for k_z is near $-k_z^2$ [see Fig. 3(c)] with $\eta = 4$. The lattice number is 4061. (g) The energy gap E_g as a function of k_z for different system size with $\eta = 4$. (h) Spectrum of the quasicrystalline system as a function of k_z near $-k_z^3$ with $\eta = 6$ [see Fig. 3(d)]. The lattice number is 2569. The parameters in (a)–(e), (f)–(g), and (h) are the same as those in Figs. 2(b), 3(c), and 3(d), respectively.

to the gap-closing point shown in Fig. 2(b). For about $-5.7 < M < 0.3$, the existence of the gap closure with the accompanying topological phase transition between $Q_{xy} = 0$ and $Q_{xy} = 0.5$ indicates that the system corresponds to the SOTSM phase. For about $M > 0.3$, the system corresponds to a 3D quasicrystalline SOTI phase with a topological gap characterized by a quantized quadrupole moment $Q_{xy} = 0.5$ for any k_z. For about $M < -5.7$, the system is a normal insulator (NI) with a topologically trivial gap.

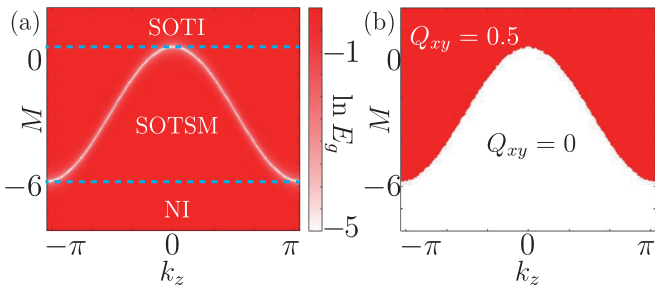

FIG. 5. (a) The logarithm of the energy gap $\ln E_g$ and (b) the quadrupole moment Q_{xy} as functions of the parameter M and the momentum k_z. In (a), each point in the white line depicts the gap-closing point. In (b), the red and white areas host a quantized quadrupole moment $Q_{xy} = 0.5$ and a zero quadrupole moment $Q_{xy} = 0$, respectively. Depending on M, the system can be divided into three phases: the SOTI phase, the SOTSM phase, and the normal insulator (NI) phase. The three phases are separated by the dashed cyan lines. The results are obtained in the AB-tiling quasicrystalline square systems with periodic boundary conditions along all the directions. The lattice site number is 1257. The parameters are $\eta = 2$, $t_2 = 1$, $g = 1$, and $t_z = 1.5$.

Above we only consider the case of $\eta = 2$ in the AB-tiling quasicrystal. In the cases of the AB-tiling octagonal quasicrystal with $\eta = 4$ and the Stampfli-tiling dodecagonal quasicrystal with $\eta = 6$, we find similar results by adjusting the parameter M, i.e., the systems also support the quasicrystalline SOTSM phase, the 3D quasicrystalline SOTI phase, and the NI phase (see Appendix B).

VI. DISCLINATION-INDUCED BOUND STATES

Disclination-induced bound states provide a potential probe of crystalline topology, which has been widely investigated in different topological systems [34,70–75]. Recently, disclination-induced bound states have been observed in topological crystalline insulators [76], acoustic topological insulators [77–80], and acoustic Weyl semimetals [81]. In this section, we study the disclination-induced bound states in the quasicrystalline SOTSM phase.

The disclination is introduced by cutting out a specific segment [the first column in Fig. 6] and then glue the lattice back together [the second column in Fig. 6]. The two sides of the cut are glued together by identifying sites on the two sides of the cut related by rotational symmetry, which is called a Volterra process [34,72,82]. The defects break the rotational symmetry locally at the center of lattice, but the rest preserves the rotational symmetry and is indistinguishable from the bulk of the original system without the cut.

The corresponding spectral function of sample geometries in Figs. 6(a) and 6(b), Figs. 6(c) and 6(d), and Figs. 6(e) and 6(f) are similar to Fig. 2(a), Fig. 3(a), and Fig. 3(b), respectively, except that the spatial probability distributions are different for the zero-energy modes. The colored points

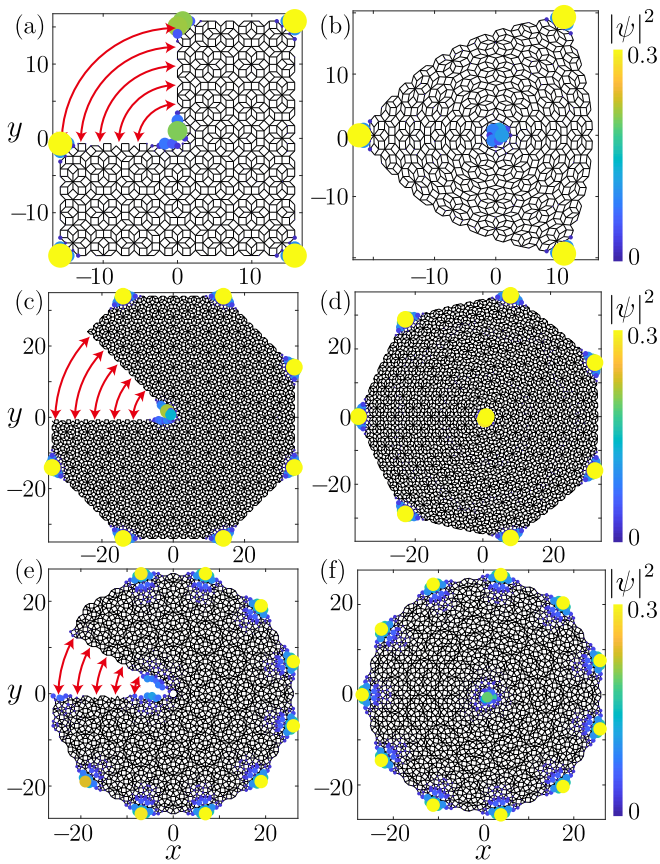

FIG. 6. Probability distributions of the zero-energy modes in the different systems with $k_z = -2$. [(a),(c),(e)] Systems with a certain segment being cut out. [(b),(d),(f)] Disclination systems where the two sides of the cut is glued together [the red lines in (a), (c), and (e)]. The parameters in [(a),(b)], [(c),(d)], and [(e),(f)] are the same as that in Fig. 2(b), Fig. 3(c), and Fig. 3(d), respectively.

in Fig. 6 display the probability distributions of the zero-energy modes in these systems with $k_z = -2$. For the three different disclination systems in Figs. 6(b), 6(d), and 6(f), they both host one zero-energy mode at the disclination core, and three, seven, and eleven zero-energy modes at the hinges of the systems, respectively. Moreover, similar to the zero-energy hinge modes, the disclination modes only appear for $|k_z| > k_z^{1/2/3}$, and disappear in the regions of $|k_z| < k_z^{1/2/3}$. This further reveals that the disclination-induced bound states and the hinge Fermi arc states are the consequence of nontrivial bulk topology, which cannot be removed without topologically trivializing the bulk of systems [34]. Moreover, the k_z-dependent disclination-induced bound states provide an experimental probe for the quasicrystalline SOTSM phase.

Usually, the fractional charge will appear around the defect core in the curved crystalline Chern insulators [83]. Fractional charges have been investigated in crystalline systems [83], and recent efforts have extended these concepts to quasicrystalline systems [26,37], by deriving the effective model for the low-energy state. The disclination-induced quasicrystalline SOTSM state may also exhibit a unique fractional hinge charge, and this will be studied in our future works.

VII. CONCLUSIONS AND DISCUSSION

In conclusion, this study has demonstrated that a stack of 2D quasicrystalline SOTIs can give rise to 3D quasicrystalline SOTSM phases. These 3D phases exhibit rotation-symmetry-protected hinge Fermi arcs, which are forbidden in crystalline systems. Additionally, our calculations have shown that the stacked systems also support the 3D quasicrystalline SOTI phase, as evidenced by the phase diagram. We have proposed that the dependence of k_z on disclination-induced bound states can serve as an experimental probe for the quasicrystalline SOTSM phase. Furthermore, considering the fivefold rotational symmetric SOTI had also been proposed [36,37], we expect that the fivefold rotational symmetric SOTSM may also be constructed by vertically stacking the fivefold rotational symmetric SOTI in a proper way.

While the quasicrystalline SOTSM shares similarities with the crystalline SODSM [9–13,16], there are three main distinctions between them. Firstly, the number of C_n^z-symmetry protected hinge Fermi arcs in the quasicrystalline SOTSM is not limited to four, as observed in crystalline SODSM, but can be eight or twelve as well. Secondly, in the quasicrystalline SOTSM, the lack of translational symmetry renders the in-plane momentum ineffective as a quantum number, making it impossible to define Dirac points in momentum space, unlike in crystalline SODSM where the Dirac equation applies. Lastly, the spectrum of the quasicrystalline SOTSM exhibits a higher number of band-crossing points compared to the crystalline SODSM, a consequence of the absence of in-plane translational symmetry in the stacked quasicrystals.

Moreover, recent experiments investigating the stack of $Ta_{1.6}Te$ quasicrystal layers [54], along with first-principles calculations and symmetry analysis, have revealed a symmetry-protected semimetal phase and explored the topological properties of the material. This suggests that the quasicrystalline SOTSM phase can be experimentally realized in real materials. Furthermore, considering the successful experimental realization of the 2D quasicrystalline SOTI phase in electrical circuit systems [41], we believe that the quasicrystalline SOTSM holds promise in metamaterials. These unique features and possibilities offer exciting prospects for the future implementation of our proposal.

Note added. Recently, we became aware of a complementary study [84], which focuses on higher-order topological insulators and semimetals in a stack of Ammann-Beenker tiling quasicrystalline lattices.

ACKNOWLEDGMENTS

D.-H.X. was supported by the NSFC (under Grants No. 12074108 and No. 12147102), the Natural Science Foundation of Chongqing (Grant No. CSTB2022NSCQ-MSX0568), and the Fundamental Research Funds for the Central Universities (Grant No. 2023CDJXY-048). R.C. acknowledges the support of the NSFC (under Grant No. 12304195) and the Chutian Scholars Program in Hubei Province. B.Z. was supported by the NSFC (under Grant No. 12074107), the program of outstanding young and middle-aged scientific and technological innovation team of colleges and universities in Hubei Province (under Grant No. T2020001) and the

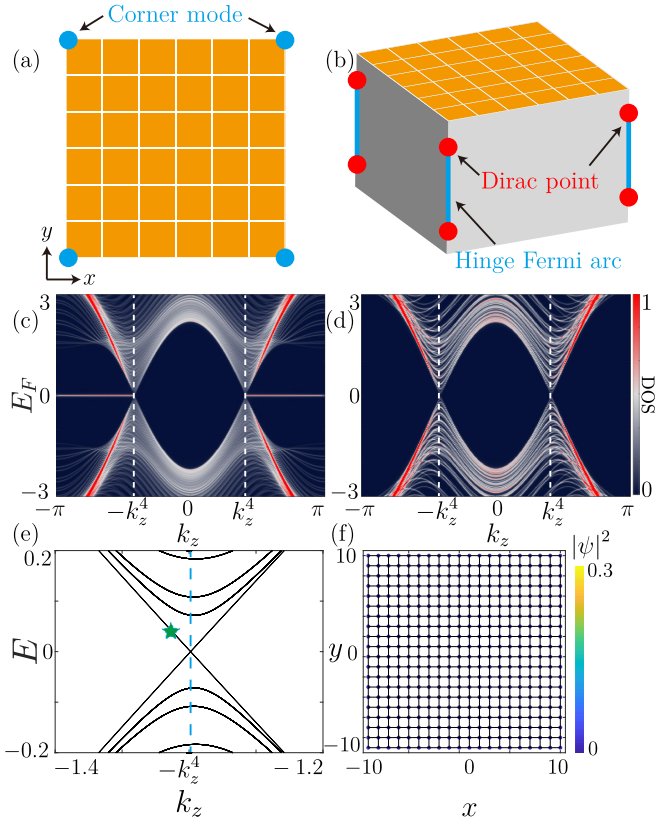

FIG. 7. (a) Schematic illustrations of the crystalline SOTI in a square lattice. The 2D crystalline system supports four rotation-symmetry-protected zero-energy corner modes (the cyan points). (b) A simple stack of the 2D crystalline system can lead to the 3D crystalline SODSM phase with four rotation-symmetry-protected hinge Fermi arc states (the cyan lines). [(c),(d)] Spectral function of the crystalline square system as a function of k_z with (c) open boundary conditions along the in-plane directions and periodic boundary condition along the z direction and (d) periodic boundary conditions along all the directions. (e) Energy spectrum of the quasicrystalline system for k_z is near $-k_z^4$. (f) Probability distribution of the states marked by the green star in (e). The parameters are taken as $\eta = 2$, $M = -2$, $t_2 = 1$, $g = 1$, and $t_z = 1.5$. The lattice number is 400.

innovation group project of the natural science foundation of Hubei Province of China (under Grant No. 2022CFA012).

APPENDIX A: CRYSTALLINE SODSM

To make a comparative study, we investigate the 3D crystalline SODSM phase [Fig. 7(b)], modeled by staking 2D crystalline SOTIs along the vertical direction [Fig. 7(a)].

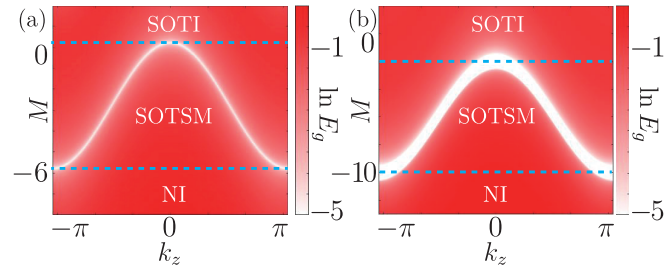

FIG. 8. The logarithm of the energy gap $\ln E_g$ as functions of the parameter M and the momentum k_z for (a) $\eta = 4$ and (b) $\eta = 6$. Each point in the white line depicts the gap-closing point. Depending on M, the system can be divided into three phases: the SOTI phase, the SOTSM phase, and the NI phase. The three phases are separated by the dashed cyan lines. The results are obtained in (a) the AB-tiling quasicrystalline and (b) Stampfli-tiling quasicrystalline systems with periodic boundary conditions along all the directions. The lattice site number is 1257 in (a) and 2569 in (b). The parameters are $t_2 = 1$, $g = 1$, and $t_z = 1.5$ in (a) and $t_2 = 2$, $g = 2$, and $t_z = 2$ in (b).

Figures 7(c) and 7(d) show the spectral function of the crystalline system with open and periodic boundary conditions in xy plane, respectively. Hinge Fermi arcs appear and connect the band-closing points at $k_z = \pm k_z^4$. The results are similar to those in Figs. 2(a) and 2(b). Figure 7(e) shows the spectrum near the band-closing point $-k_c^4$. Only one band-crossing point is observed because of the existence of transitional symmetry in crystalline systems. This is observed more clearly in Fig. 7(f). The probability distribution of the state labeled by green star [Fig. 7(e)] is uniformly distributed and all the local patches undergo the topological phase transition simultaneously when k_z varies. Moreover, we find that the low-energy effective Hamiltonian can be described by the massless Dirac equation. Therefore, the system is identified as the crystalline SODSM phase.

APPENDIX B: PHASE DIAGRAM FOR $\eta = 4$ AND 6

Figures 8(a) and 8(b) show the phase diagram for the cases of the AB-tiling octagonal quasicrystal with $\eta = 4$ and the Stampfli-tiling dodecagonal quasicrystal with $\eta = 6$, respectively. We find similar results by adjusting the parameter M, except that there appear more white regions in Fig. 8(b) because it hosts more band-crossing points [see Fig. 4(f)]. Furthermore, well-defined topological numbers for the systems with $\eta = 4$ and $\eta = 6$ are both intriguing and demanding to ascertain. Therefore, we are unable to provide topological numbers for the phase diagrams.

[1] W. A. Benalcazar, B. A. Bernevig, and T. L. Hughes, Quantized electric multipole insulators, Science **357**, 61 (2017).

[2] F. Schindler, A. M. Cook, M. G. Vergniory, Z. Wang, S. S. P. Parkin, B. A. Bernevig, and T. Neupert, Higher-order topological insulators, Sci. Adv. **4**, eaat0346 (2018).

[3] J. Langbehn, Y. Peng, L. Trifunovic, F. von Oppen, and P. W. Brouwer, Reflection-symmetric second-order topological insulators and superconductors, Phys. Rev. Lett. **119**, 246401 (2017).

[4] W. A. Benalcazar, B. A. Bernevig, and T. L. Hughes, Electric multipole moments, topological multipole moment pumping, and chiral hinge states in crystalline insulators, Phys. Rev. B **96**, 245115 (2017).

[5] Z. Song, Z. Fang, and C. Fang, $(d-2)$-dimensional edge states of rotation symmetry protected topological states, Phys. Rev. Lett. **119**, 246402 (2017).

[6] C.-Z. Li, A.-Q. Wang, C. Li, W.-Z. Zheng, A. Brinkman, D.-P. Yu, and Z.-M. Liao, Reducing electronic transport dimension to

topological hinge states by increasing geometry size of Dirac semimetal Josephson junctions, Phys. Rev. Lett. **124**, 156601 (2020).

[7] A. C. Tyner, S. Sur, Q. Zhou, D. Puggioni, P. Darancet, J. M. Rondinelli, and P. Goswami, Non-Abelian Stokes theorem and quantized Berry flux, arXiv:2102.06207

[8] S. Nie, J. Chen, C. Yue, C. Le, D. Yuan, Z. Wang, W. Zhang, and H. Weng, Tunable Dirac semimetals with higher-order Fermi arcs in Kagome lattices $Pd_3Pb_2X_2$ (X=S,Se), Sci. Bull. **67**, 1958 (2022).

[9] Y. Fang and J. Cano, Classification of Dirac points with higher-order Fermi arcs, Phys. Rev. B **104**, 245101 (2021).

[10] B. J. Wieder, Z. Wang, J. Cano, X. Dai, L. M. Schoop, B. Bradlyn, and B. A. Bernevig, Strong and fragile topological Dirac semimetals with higher-order Fermi arcs, Nat. Commun. **11**, 627 (2020).

[11] X.-T. Zeng, Z. Chen, C. Chen, B.-B. Liu, X.-L. Sheng, and S. A. Yang, Topological hinge modes in Dirac semimetals, Front. Phys. **18**, 13308 (2023).

[12] A. L. Szabó and B. Roy, Dirty higher-order Dirac semimetal: Quantum criticality and bulk-boundary correspondence, Phys. Rev. Res. **2**, 043197 (2020).

[13] M. Lin and T. L. Hughes, Topological quadrupolar semimetals, Phys. Rev. B **98**, 241103(R) (2018).

[14] R. Chen, T. Liu, C. M. Wang, H.-Z. Lu, and X. C. Xie, Field-tunable one-sided higher-order topological hinge states in Dirac semimetals, Phys. Rev. Lett. **127**, 066801 (2021).

[15] Z.-M. Wang, R. Wang, J.-H. Sun, T.-Y. Chen, and D.-H. Xu, Floquet Weyl semimetal phases in light-irradiated higher-order topological Dirac semimetals, Phys. Rev. B **107**, L121407 (2023).

[16] K. Wang, J.-X. Dai, L. B. Shao, S. A. Yang, and Y. X. Zhao, Boundary criticality of $\mathcal{PT}$-invariant topology and second-order nodal-line semimetals, Phys. Rev. Lett. **125**, 126403 (2020).

[17] H.-X. Wang, Z.-K. Lin, B. Jiang, G.-Y. Guo, and J.-H. Jiang, Higher-order Weyl semimetals, Phys. Rev. Lett. **125**, 146401 (2020).

[18] S. A. A. Ghorashi, T. Li, and T. L. Hughes, Higher-order Weyl semimetals, Phys. Rev. Lett. **125**, 266804 (2020).

[19] D.-T. Tran, A. Dauphin, N. Goldman, and P. Gaspard, Topological Hofstadter insulators in a two-dimensional quasicrystal, Phys. Rev. B **91**, 085125 (2015).

[20] C. W. Duncan, S. Manna, and A. E. B. Nielsen, Topological models in rotationally symmetric quasicrystals, Phys. Rev. B **101**, 115413 (2020).

[21] Z. Li and Z. F. Wang, Quantum anomalous Hall effect in twisted bilayer graphene quasicrystal, Chin. Phys. B **29**, 107101 (2020).

[22] J. Jeon, M. J. Park, and S. B. Lee, Length scale formation in the Landau levels of quasicrystals, Phys. Rev. B **105**, 045146 (2022).

[23] A.-L. He, L.-R. Ding, Y. Zhou, Y.-F. Wang, and C.-D. Gong, Quasicrystalline Chern insulators, Phys. Rev. B **100**, 214109 (2019).

[24] S. Traverso, M. Sassetti, and N. T. Ziani, Role of the edges in a quasicrystalline Haldane model, Phys. Rev. B **106**, 125428 (2022).

[25] H. Huang and F. Liu, Quantum spin Hall effect and spin Bott index in a quasicrystal lattice, Phys. Rev. Lett. **121**, 126401 (2018).

[26] S. Spurrier and N. R. Cooper, Kane-Mele with a twist: Quasicrystalline higher-order topological insulators with fractional mass kinks, Phys. Rev. Res. **2**, 033071 (2020).

[27] M. A. Bandres, M. C. Rechtsman, and M. Segev, Topological photonic quasicrystals: Fractal topological spectrum and protected transport, Phys. Rev. X **6**, 011016 (2016).

[28] K. Pöyhönen, I. Sahlberg, A. Westström, and T. Ojanen, Amorphous topological superconductivity in a Shiba glass, Nat. Commun. **9**, 2103 (2018).

[29] I. C. Fulga, D. I. Pikulin, and T. A. Loring, Aperiodic weak topological superconductors, Phys. Rev. Lett. **116**, 257002 (2016).

[30] S. Manna, S. K. Das, and B. Roy, Noncrystalline topological superconductors, arXiv:2207.02203.

[31] S. Longhi, Topological phase transition in non-Hermitian quasicrystals, Phys. Rev. Lett. **122**, 237601 (2019).

[32] Q.-B. Zeng, Y.-B. Yang, and Y. Xu, Topological phases in non-Hermitian Aubry-André-Harper models, Phys. Rev. B **101**, 020201(R) (2020).

[33] R. Chen, C.-Z. Chen, J.-H. Gao, B. Zhou, and D.-H. Xu, Higher-order topological insulators in quasicrystals, Phys. Rev. Lett. **124**, 036803 (2020).

[34] D. Varjas, A. Lau, K. Pöyhönen, A. R. Akhmerov, D. I. Pikulin, and I. C. Fulga, Topological phases without crystalline counterparts, Phys. Rev. Lett. **123**, 196401 (2019).

[35] C.-B. Hua, R. Chen, B. Zhou, and D.-H. Xu, Higher-order topological insulator in a dodecagonal quasicrystal, Phys. Rev. B **102**, 241102(R) (2020).

[36] H. Huang, J. Fan, D. Li, and F. Liu, Generic orbital design of higher-order topological quasicrystalline insulators with odd five-fold rotation symmetry, Nano Lett. **21**, 7056 (2021).

[37] C. Wang, F. Liu, and H. Huang, Effective model for fractional topological corner modes in quasicrystals, Phys. Rev. Lett. **129**, 056403 (2022).

[38] A. Shi, J. Jiang, Y. Peng, P. Peng, J. Chen, and J. Liu, Multimer analysis method reveals higher-order topology in quasicrystals, arXiv:2209.05751.

[39] L. Xiong, Y. Zhang, Y. Liu, Y. Zheng, and X. Jiang, Higher-order topological states in photonic Thue-Morse quasicrystals: Quadrupole insulator and a new origin of corner states, arXiv:2207.12286.

[40] R. Ghadimi, T. Sugimoto, K. Tanaka, and T. Tohyama, Topological superconductivity in quasicrystals, Phys. Rev. B **104**, 144511 (2021).

[41] B. Lv, R. Chen, R. Li, C. Guan, B. Zhou, G. Dong, C. Zhao, Y. Li, Y. Wang, H. Tao, J. Shi, and D.-H. Xu, Realization of quasicrystalline quadrupole topological insulators in electrical circuits, Commun. Phys. **4**, 108 (2021).

[42] R. Chen, D.-H. Xu, and B. Zhou, Topological Anderson insulator phase in a quasicrystal lattice, Phys. Rev. B **100**, 115311 (2019).

[43] C.-B. Hua, Z.-R. Liu, T. Peng, R. Chen, D.-H. Xu, and B. Zhou, Disorder-induced chiral and helical Majorana edge modes in a two-dimensional Ammann-Beenker quasicrystal, Phys. Rev. B **104**, 155304 (2021).

[44] T. Peng, C.-B. Hua, R. Chen, D.-H. Xu, and B. Zhou, Topological Anderson insulators in an Ammann-Beenker quasicrystal and a snub-square crystal, Phys. Rev. B **103**, 085307 (2021).

[45] T. Peng, C.-B. Hua, R. Chen, Z.-R. Liu, D.-H. Xu, and B. Zhou, Higher-order topological Anderson insulators in quasicrystals, Phys. Rev. B **104**, 245302 (2021).

[46] M. Verbin, O. Zilberberg, Y. E. Kraus, Y. Lahini, and Y. Silberberg, Observation of topological phase transitions in photonic quasicrystals, Phys. Rev. Lett. **110**, 076403 (2013).

[47] D. J. Apigo, W. Cheng, K. F. Dobiszewski, E. Prodan, and C. Prodan, Observation of topological edge modes in a quasiperiodic acoustic waveguide, Phys. Rev. Lett. **122**, 095501 (2019).

[48] D. Shechtman, I. Blech, D. Gratias, and J. W. Cahn, Metallic phase with long-range orientational order and no translational symmetry, Phys. Rev. Lett. **53**, 1951 (1984).

[49] D. Levine and P. J. Steinhardt, Quasicrystals: A new class of ordered structures, Phys. Rev. Lett. **53**, 2477 (1984).

[50] B. D. Biggs, S. J. Poon, and N. R. Munirathnam, Stable Al-Cu-Ru icosahedral crystals: A new class of electronic alloys, Phys. Rev. Lett. **65**, 2700 (1990).

[51] F. S. Pierce, S. J. Poon, and Q. Guo, Electron localization in metallic quasicrystals, Science **261**, 737 (1993).

[52] D. N. Basov, F. S. Pierce, P. Volkov, S. J. Poon, and T. Timusk, Optical conductivity of insulating Al-based alloys: Comparison of quasiperiodic and periodic systems, Phys. Rev. Lett. **73**, 1865 (1994).

[53] F. S. Pierce, Q. Guo, and S. J. Poon, Enhanced insulatorlike electron transport behavior of thermally tuned quasicrystalline states of Al-Pd-Re alloys, Phys. Rev. Lett. **73**, 2220 (1994).

[54] J. D. Cain, A. Azizi, M. Conrad, S. M. Griffin, and A. Zettl, Layer-dependent topological phase in a two-dimensional quasicrystal and approximant, Proc. Natl. Acad. Sci. USA **117**, 26135 (2020).

[55] A. G. e. Fonseca, T. Christensen, J. D. Joannopoulos, and M. Soljačić, Quasicrystalline Weyl points and dense Fermi-Bragg arcs, Phys. Rev. B **108**, L121109 (2023).

[56] A. A. Burkov and L. Balents, Weyl semimetal in a topological insulator multilayer, Phys. Rev. Lett. **107**, 127205 (2011).

[57] M. Mogi, M. Kawamura, R. Yoshimi, A. Tsukazaki, Y. Kozuka, N. Shirakawa, K. S. Takahashi, M. Kawasaki, and Y. Tokura, A magnetic heterostructure of topological insulators as a candidate for an axion insulator, Nat. Mater. **16**, 516 (2017).

[58] M. Mogi, M. Kawamura, A. Tsukazaki, R. Yoshimi, K. S. Takahashi, M. Kawasaki, and Y. Tokura, Tailoring tricolor structure of magnetic topological insulator for robust axion insulator, Sci. Adv. **3**, eaao1669 (2017).

[59] Y. Deng, Y. Yu, M. Z. Shi, Z. Guo, Z. Xu, J. Wang, X. H. Chen, and Y. Zhang, Quantum anomalous Hall effect in intrinsic magnetic topological insulator $MnBi_2Te_4$, Science **367**, 895 (2020).

[60] A. Gao, Y.-F. Liu, C. Hu, J.-X. Qiu, C. Tzschaschel, B. Ghosh, S.-C. Ho, D. Bérubé, R. Chen, H. Sun *et al.*, Layer Hall effect in a 2D topological axion antiferromagnet, Nature (London) **595**, 521 (2021).

[61] R. Chen, S. Li, H.-P. Sun, Q. Liu, Y. Zhao, H.-Z. Lu, and X. C. Xie, Using nonlocal surface transport to identify the axion insulator, Phys. Rev. B **103**, L241409 (2021).

[62] Y.-R. Ding, D.-H. Xu, C.-Z. Chen, and X. C. Xie, Hinged quantum spin Hall effect in antiferromagnetic topological insulators, Phys. Rev. B **101**, 041404(R) (2020).

[63] N. Shumiya, M. S. Hossain, J.-X. Yin, Z. Wang, M. Litskevich, C. Yoon, Y. Li, Y. Yang, Y.-X. Jiang, G. Cheng *et al.*, Evidence of a room-temperature quantum spin Hall edge state in a higher-order topological insulator, Nat. Mater. **21**, 1111 (2022).

[64] Y.-F. Zhao, R. Zhang, R. Mei, L.-J. Zhou, H. Yi, Y.-Q. Zhang, J. Yu, R. Xiao, K. Wang, N. Samarth *et al.*, Tuning the Chern number in quantum anomalous Hall insulators, Nature (London) **588**, 419 (2020).

[65] A. Agarwala, V. Juričić, and B. Roy, Higher-order topological insulators in amorphous solids, Phys. Rev. Res. **2**, 012067(R) (2020).

[66] Y.-L. Tao and Y. Xu, Higher-order topological hyperbolic lattices, Phys. Rev. B **107**, 184201 (2023).

[67] B. Roy, Antiunitary symmetry protected higher-order topological phases, Phys. Rev. Res. **1**, 032048(R) (2019).

[68] J. H. Pixley, D. A. Huse, and S. Das Sarma, Rare-region-induced avoided quantum criticality in disordered three-dimensional Dirac and Weyl semimetals, Phys. Rev. X **6**, 021042 (2016).

[69] B. Roy, R.-J. Slager, and V. Juričić, Global phase diagram of a dirty Weyl liquid and emergent superuniversality, Phys. Rev. X **8**, 031076 (2018).

[70] W. A. Benalcazar, T. Li, and T. L. Hughes, Quantization of fractional corner charge in C_n-symmetric higher-order topological crystalline insulators, Phys. Rev. B **99**, 245151 (2019).

[71] G. van Miert and C. Ortix, Dislocation charges reveal two-dimensional topological crystalline invariants, Phys. Rev. B **97**, 201111(R) (2018).

[72] M. Geier, I. C. Fulga, and A. Lau, Bulk-boundary-defect correspondence at disclinations in rotation-symmetric topological insulators and superconductors, SciPost Phys. **10**, 092 (2021).

[73] Y. Qi, H. He, and M. Xiao, Manipulation of acoustic vortex with topological dislocation states, Appl. Phys. Lett. **120**, 212202 (2022).

[74] R.-J. Slager, A. Mesaros, V. Juričić, and J. Zaanen, The space group classification of topological band-insulators, Nat. Phys. **9**, 98 (2013).

[75] R.-J. Slager, The translational side of topological band insulators, J. Phys. Chem. Solids **128**, 24 (2019).

[76] C. W. Peterson, T. Li, W. Jiang, T. L. Hughes, and G. Bahl, Trapped fractional charges at bulk defects in topological insulators, Nature (London) **589**, 376 (2021).

[77] L. Ye, C. Qiu, M. Xiao, T. Li, J. Du, M. Ke, and Z. Liu, Topological dislocation modes in three-dimensional acoustic topological insulators, Nat. Commun. **13**, 508 (2022).

[78] H. Xue, D. Jia, Y. Ge, Y.-j. Guan, Q. Wang, S.-q. Yuan, H.-x. Sun, Y. D. Chong, and B. Zhang, Observation of dislocation-induced topological modes in a three-dimensional acoustic topological insulator, Phys. Rev. Lett. **127**, 214301 (2021).

[79] Y. Deng, W. A. Benalcazar, Z.-G. Chen, M. Oudich, G. Ma, and Y. Jing, Observation of degenerate zero-energy topological states at disclinations in an acoustic lattice, Phys. Rev. Lett. **128**, 174301 (2022).

[80] B. Xia, Z. Jiang, L. Tong, S. Zheng, and X. Man, Topological bound states in elastic phononic plates induced by disclinations, Acta Mech. Sin. **38**, 521459 (2022).

[81] Q. Wang, Y. Ge, H. xiang Sun, H. Xue, D. Jia, Y. jun Guan, S. qi Yuan, B. Zhang, and Y. D. Chong, Vortex states in an acoustic Weyl crystal with a topological lattice defect, Nat. Commun. **12**, 3654 (2021).

[82] M. Kleman and J. Friedel, Disclinations, dislocations, and continuous defects: A reappraisal, Rev. Mod. Phys. **80**, 61 (2008).

[83] T. Li, P. Zhu, W. A. Benalcazar, and T. L. Hughes, Fractional disclination charge in two-dimensional C_n-symmetric topological crystalline insulators, Phys. Rev. B **101**, 115115 (2020).

[84] Y.-F. Mao, Y.-L. Tao, J.-H. Wang, Q.-B. Zeng, and Y. Xu, Higher-order topological insulators and semimetals in three dimensions without crystalline counterparts, arXiv:2307.14974.